

AugMapNet: Improving Spatial Latent Structure via BEV Grid Augmentation for Enhanced Vectorized Online HD Map Construction

Thomas Monninger^{1,2}, Md Zafar Anwar¹, Stanislaw Antol¹, Steffen Staab^{2,3}, Sihao Ding¹

¹Mercedes-Benz Research & Development North America, Sunnyvale, CA, USA

²University of Stuttgart, Institute for Artificial Intelligence, Stuttgart, Germany

³University of Southampton, Southampton, United Kingdom

Abstract

Autonomous driving requires an understanding of the infrastructure elements, such as lanes and crosswalks. To navigate safely, this understanding must be derived from sensor data in real-time and needs to be represented in vectorized form. Learned Bird's-Eye View (BEV) encoders are commonly used to combine a set of camera images from multiple views into one joint latent BEV grid. Traditionally, from this latent space, an intermediate raster map is predicted, providing dense spatial supervision but requiring post-processing into the desired vectorized form. More recent models directly derive infrastructure elements as polylines using vectorized map decoders, providing instance-level information. Our approach, **Augmentation Map Network (AugMapNet)**, proposes latent BEV grid augmentation, a novel technique that significantly enhances the latent BEV representation. AugMapNet combines vector decoding and dense spatial supervision more effectively than existing architectures while remaining as straightforward to integrate and as generic as auxiliary supervision. Experiments on nuScenes and Argoverse2 datasets demonstrate significant improvements in vectorized map prediction performance up to 13.3% over the StreamMapNet baseline on 60m range and greater improvements on larger ranges. We confirm transferability by applying our method to another baseline and find similar improvements. A detailed analysis of the latent BEV grid confirms a more structured latent space of AugMapNet and shows the value of our novel concept beyond pure performance improvement. The code will be released soon.

1. Introduction

Autonomous driving relies on an accurate representation of the static infrastructure surrounding the autonomous vehicle to understand the environment and make informed decisions. Typically, a High-Definition (HD) map is given *a priori* to capture essential information such as lanes, dividers, crosswalks, and other static elements. However,

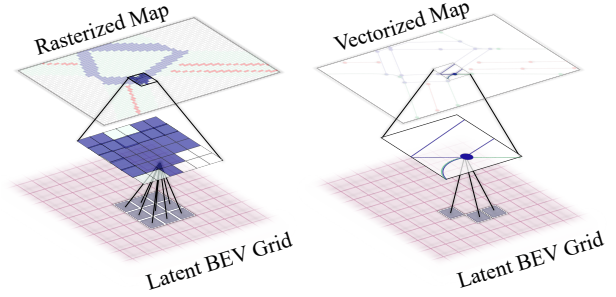


Figure 1. Schematic relation between output element and latent BEV grid. Rasterized decoding (left) and vectorized decoding (right) provide dense and sparse spatial supervision, respectively.

since the real world is subject to change due to events such as construction, road closures, or weather conditions, relying solely on offline HD maps may not always be safe. To address this, the construction of online maps from the perception system is essential to ensure safety.

An online HD map informs the autonomous vehicle about its environment in real time. Maps represent characteristics of the traffic scene, which static traffic elements may not be fully defined. For example, defining lanes purely based on the visible markings might fail in case of their absence. Hence, characteristics of the traffic scene must be derived from the infrastructure context, which requires a holistic semantic understanding of the traffic scene. In the case of lanes, other infrastructure elements, such as curbs or guardrails, must be considered.

Furthermore, most autonomous vehicle systems require the map in vectorized form for use in their planning system, since a vectorized representation provides instance-level information and spatial consistency [7, 19, 21].

Related works for online HD map construction commonly perform pixel-level semantic segmentation in a 2D top-down view to predict a Bird's-Eye View (BEV) raster map [15, 26, 29]. A vectorized representation can be derived from this intermediate raster map representation in a post-processing step [14]. Recent approaches [19, 21, 38] introduce vector map decoding to predict the spatial po-

sition of static elements with polylines and, thus, directly generate the vectorized representation of the target.

Both paradigms leverage the same learned BEV encoder concept that fuses data from multiple sensors into one joint latent BEV grid [29], which is a spatial grid representation of the environment encoded in the latent feature space of a neural network. However, as shown in Fig. 1, rasterized map decoders (left) and vectorized map decoders (right) have different extents of spatial supervision, which is discussed below. First, raster map decoders predict a pixel-level classification. Outputs and labels are both dense rasters, providing a dense pixel-wise loss for optimization. In contrast, vector decoders have sparse outputs and labels relative to the raster map representation, resulting in reduced guidance from the sparse loss.

Secondly, raster map decoders typically use convolutional layers, where each cell in the latent BEV grid contributes to the output. In contrast, vector map decoders typically use deformable attention-based mechanisms, such as deformable DETR [42], where only a subset of cells from the latent BEV grid contributes to the output. Therefore, in a single step, training a raster map decoder optimizes all cells in the latent BEV grid, but training a vector map decoder optimizes only a subset. We refer to these properties of raster map decoders as dense spatial supervision, in contrast to the sparse supervision of vector map decoders.

Based on this reasoning, we argue that including dense spatial supervision in the learning task provides additional guidance for deriving the high-quality vectorized HD map. A common approach is adding an auxiliary semantic segmentation task [6, 13, 19]. However, more sophisticated techniques can increase performance further [39]. We propose a novel latent BEV augmentation method that directly injects dense spatial features from an intermediate raster map into the latent BEV grid. We further propose gradient stopping to treat the predicted raster map as an immutable prior. To verify our method, we implement AugMapNet, a model that leverages latent BEV grid augmentation to enhance the performance of vector map decoders. We confirm transferability by applying our method to another baseline.

In summary, the main contributions of this paper are:

- We propose a novel latent BEV grid augmentation method that combines vector decoding and dense spatial supervision while remaining as straightforward to integrate and as generic as auxiliary supervision.
- We develop a new model, AugMapNet, that combines latent augmentation and gradient stopping, and demonstrate its effectiveness through extensive experiments on two datasets and on multiple perception ranges. We further show transferability to another baseline.
- We show that applying our method significantly enhances the structure in the latent BEV grid, which correlates with improved vector map decoding performance.

2. Related Work

2.1. Rasterized Map Construction

One option to represent map elements is a rasterized form (Fig. 1, left). Phillion and Fidler [29] proposed the first learning-based architecture for online raster map construction from camera images by performing pixel-wise classification using semantic segmentation. BEVFormer [15] improves segmentation accuracy by aggregating temporal information across multiple time steps, opening a line of work. BEVFormer v2 [37] and BEVDet4D [10] use a concatenation-based temporal aggregation strategy, VideoBEV [8] and StreamPETR [34] leverage recurrent temporal aggregation methods, and SoloFusion [27] and TempBEV [25] investigate temporal aggregation along various time frames and feature spaces. Similar to previous approaches, HDMapNet [14] performs semantic segmentation first, but adds a post-processing step second to derive a vectorized representation. While raster map prediction leads to dense spatial supervision, post-processing is required to get a vectorized form with instance-level information [19, 21], which is typically based on heuristics and restricts scalability and performance [14, 21]. In AugMapNet, we directly predict vectorized representations and still utilize dense spatial supervision by using latent BEV grid augmentation.

2.2. Vectorized Map Construction

Recent approaches directly predict the vectorized representation of map elements. Early works focus on topology and limit themselves to only lane centerlines [2, 23, 43]. VectorMapNet [21] is the first end-to-end model to showcase the benefit of directly predicting a vectorized map representation including drivable areas, boundaries, dividers, and crosswalks. MapTR [19] addresses the ambiguity in selecting a discrete set of points to model geometries in vectorized representations by employing permutation-equivalent modeling, which stabilizes the learning process. StreamMapNet [38] improves vector map decoding by introducing memory buffers to achieve temporal stability, aiding in the construction of long-range, local HD maps.

All recent vector map decoders [19, 21, 38] share the same underlying deformable DETR [42] mechanism for decoding (see Fig. 1, right). Its deformable attention mechanism samples K keys as a subset of all the latent BEV grid feature vectors. Only a subset of the BEV grid cells contribute to the sparse vectorized output, leading to sparse spatial supervision. Hence, this type of vector map decoders is expected to exhibit a latent space with less spatial structure as compared to raster map decoders. In AugMapNet, we extend existing models with a novel latent BEV grid augmentation method to combine the benefits of direct vectorized prediction and dense spatial supervision.

2.3. Latent Space Supervision and Analysis

A straightforward approach to add spatial supervision is by adding an auxiliary semantic segmentation task, as done by PivotNet [6], MapTRv2 [19], and SeaBird [13]. MapVR [39] adds a differentiable rasterizer on top of a vector map decoder only for training. A downstream auxiliary segmentation loss provides supervision directly to the vectorized output. We extend their argument that more sophisticated techniques can increase performance beyond pure auxiliary supervision [39] by introducing the AugMapNet approach, where the segmentation loss does not backpropagate to the latent BEV grid and is therefore not an auxiliary loss.

Two recent works also leverage a raster representation beyond auxiliary supervision. HlMap [41] introduces a hybrid representation that jointly decodes both raster and vector outputs. In contrast, we adopt a two-stage approach in which raster decoding preconditions subsequent vector decoding. MGMap [20] likewise employs a two-stage strategy, generating an intermediate rasterized representation from which the vectorized map is predicted. However, in two-stage designs, the raster output can become a high-frequency latent space [5]. To address this, we apply gradient stopping to treat the intermediate representation as an independent prior. In summary, our mechanism combines raster and vector representations better than other hybrid architectures, while being as straightforward to integrate and as generic as auxiliary supervision. It augments the latent BEV space and preconditions the vector map decoding, which adds more structure to the final latent BEV grid.

We support our claims via analysis and visualizations on the latent BEV grid features with PCA [9]. Since our evaluation already demonstrates that learning a non-linear decoder on these latent features results in superior metric scores, we opt for the simplicity of PCA instead of non-linear approaches, such as t-SNE [33] and UMAP [22].

Other works in related tasks leverage latent BEV grid visualizations, but often do not analyze the latent BEV grid for further insights into their mechanisms. SA-BEV [40], which proposes a pooling mechanism to improve the semantics of the latent BEV grid features, and BEV-SAN [3], which adds height slices to the BEV grid, only visualize each cell’s feature vector norm to produce a grayscale image without additional quantitative analysis. FB-BEV [16] uses RGB BEV feature visualizations to support its claims, but lacks details on how BEV features are reduced to RGB and also lacks analysis of the BEV features.

Instead of cameras, some works that visualize and analyze latent features use LiDAR input. Range image visualizations rely on t-SNE in RangeRCNN [17], whereas others [28, 31] use t-SNE to show class-colored latent features that form distinct clusters. Perez *et al.* [28] analyze their BEV features via the average relative distances between classes, whereas we use the mean Silhouette score [30].

3. Approach

3.1. Problem Statement

Let $U = \{u_1, \dots, u_n\}$ be the set of image frames from the n monocular cameras mounted on the autonomous vehicle. Let $\mathcal{M}_{\text{vector}} = \{P_{\text{div}}, P_{\text{bound}}, P_{\text{ped}}\}$ be the local HD map with the autonomous vehicle at the origin, where P_{div} , P_{bound} , and P_{ped} are the sets of polylines representing lane dividers, road boundaries, and pedestrian crossings within the scene, respectively. Each polyline $P_k = [(x_i, y_i)]_{i=1}^{N_{P_k}}$ is a sequence of N_{P_k} points. The goal is to find a function f that predicts the local vectorized HD map $\hat{\mathcal{M}}_{\text{vector}}$ from the set of image frames U , *i.e.*, $\hat{\mathcal{M}}_{\text{vector}} = f(U)$. The function f is typically realized in an encoder-decoder fashion [14, 19, 21, 38]. An encoder e_{BEV} generates the latent BEV grid B , *i.e.*, $B = e_{\text{BEV}}(U)$. A decoder d_{vector} performs vector decoding into the local HD map representation, *i.e.*, $\hat{\mathcal{M}}_{\text{vector}} = d_{\text{vector}}(B)$.

3.2. Latent BEV Grid Augmentation

First, we provide a mathematical framework for the terms “dense” and “sparse” spatial supervision. Generally, the loss is calculated over all elements of the output representation $\hat{\mathcal{M}}$. Supervision for a step is done by optimizing learnable weights W based on the gradients of the loss:

$$\frac{\partial L}{\partial W} = \frac{\partial L}{\partial \hat{\mathcal{M}}} \frac{\partial \hat{\mathcal{M}}}{\partial W}. \quad (1)$$

The total amount of spatial supervision therefore is related to the number of elements in $\hat{\mathcal{M}}$. In the case of a raster map decoder, the total gradient signal is calculated from the dense loss over all pixels of the raster map ($\mathbb{R}^{H \times W}$), which gives the total number of elements:

$$|\hat{\mathcal{M}}_{\text{raster}}| = H \times W. \quad (2)$$

In the case of a vector map decoder, the total gradient signal is calculated from the sparse loss over N_p points of N polylines. The number of elements providing supervision is at most:

$$|\hat{\mathcal{M}}_{\text{vector}}| = N \times N_p. \quad (3)$$

In typical settings, such as AugMapNet, this inequality generally holds:

$$|\hat{\mathcal{M}}_{\text{raster}}| > |\hat{\mathcal{M}}_{\text{vector}}|. \quad (4)$$

This quantifies the benefit of dense spatial supervision (see more details in Supplementary B). Note that, in DETR-style decoders, out of N predicted elements, the ones correctly predicted as empty class do not induce spatial supervision. Hence, this number is the upper bound and the actual supervision is typically much sparser in a single step.

Given this motivation for dense spatial supervision, the goal is to combine this with decoding a vector map representation. To this end, we propose a novel concept of augmenting the latent BEV grid B with additional information

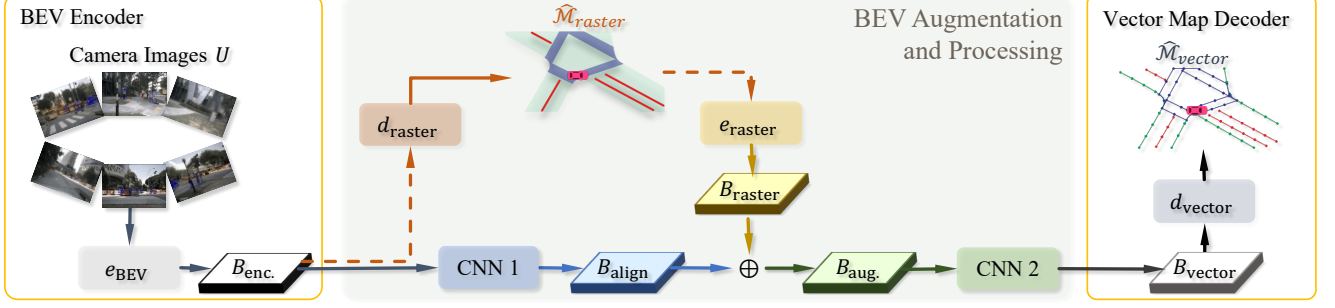


Figure 2. Overview of AugMapNet architecture. Camera images U are processed by learned BEV encoder e_{BEV} into latent BEV grid B_{enc} . AugMapNet employs a latent BEV grid augmentation mechanism that generates \hat{M}_{raster} (*i.e.*, map semantic segmentation). Additional CNNs help structure the latent space. A vector map decoder d_{vector} predicts vectorized map \hat{M}_{vector} . Dashed lines indicate gradient stop.

from a predicted raster map. During training, we rasterize the ground truth $\mathcal{M}_{\text{vector}}$ into $\mathcal{M}_{\text{raster}}$ and train a parallel raster map decoder to predict $\hat{\mathcal{M}}_{\text{raster}}$. Given an encoder e_{raster} that preserves the spatial structure, the BEV augmentation mechanism is defined as:

$$B_{\text{aug}} = B + e_{\text{raster}}(\hat{\mathcal{M}}_{\text{raster}}). \quad (5)$$

By injecting the spatial features into the latent BEV grid, we expect to enhance its spatial structure. Directly adding the encoded spatial features is expected to have a stronger impact than auxiliary supervision. B_{aug} is then used instead of B in the vector map decoder to produce the final prediction.

3.3. AugMapNet Model Architecture

We design a novel model, AugMapNet, to demonstrate the benefit of our proposed latent BEV grid augmentation concept. The full architecture is shown in Fig. 2. On a high level, AugMapNet extends any given encoder-decoder structure with e_{BEV} and d_{vector} with a BEV space augmentation. Starting on the input side, AugMapNet uses a learned BEV encoder e_{BEV} to encode given camera images U into the BEV grid B_{enc} . We add a parallel rasterized map decoder d_{raster} that predicts the rasterized map $\hat{\mathcal{M}}_{\text{raster}}$ from B_{enc} . Following the BEV augmentation concept from Eq. (5), $\hat{\mathcal{M}}_{\text{raster}}$ is encoded by e_{raster} and added back to the latent BEV grid B_{enc} , resulting in the augmented BEV grid B_{aug} . We introduce additional BEV processing with 2 CNNs to better leverage B_{raster} . CNN1 transforms B_{enc} into an aligned BEV grid, B_{align} , before it is augmented by B_{raster} . CNN2 operates on B_{aug} to combine the summed features into new latent space features in B_{align} . The benefit of these CNNs is demonstrated in Sec. 4.7, where ablations are done without the CNNs. The final latent BEV grid representation, B_{vector} , is passed to the vector map decoder d_{vector} to extract the vectorized map representation $\hat{\mathcal{M}}_{\text{vector}}$, comprising polylines P_{div} , P_{bound} , and P_{ped} .

3.4. Loss and Gradient Stopping

The vector map decoder loss ($\mathcal{L}_{\text{vector}}$) is the same as in StreamMapNet [38] and consists of a polyline matching loss ($\mathcal{L}_{\text{line}}$), a focal loss ($\mathcal{L}_{\text{focal}}$), and a transformation loss ($\mathcal{L}_{\text{trans}}$). For the raster map decoder loss ($\mathcal{L}_{\text{raster}}$), we perform semantic segmentation using the Dice loss [24]. Supplementary C has the mathematical definition of all losses.

Optimizing a parallel raster representation similar to MGMap [20] poses the risk of creating a high-frequency latent space due to the superimposed vector map decoder loss, which can hinder interpretability (*cf.* [5]). To mitigate this issue, our latent BEV grid augmentation mechanism introduces gradient stopping, as illustrated by the dashed lines in Fig. 2. This way, the vector decoding task is decoupled from the semantic segmentation task. Specifically, gradients are not backpropagated from d_{raster} to e_{BEV} to ensure that the semantic segmentation task does not affect the latent BEV grid B_{enc} and hence does not compromise the vector map decoding performance. Furthermore, gradients are not backpropagated from e_{raster} to d_{raster} to avoid d_{raster} using the rasterized map prediction $\hat{\mathcal{M}}_{\text{raster}}$ as a high-frequency latent space for vector map features. The vector decoder treats the predicted rasterized map as an immutable prior and e_{raster} learns how to generate features that are useful for the vector map decoding task. Different variations of gradient stopping are evaluated in Sec. 4.7.

3.5. Structure of Latent BEV Grid

We hypothesize that our latent BEV augmentation induces a more structured latent space due to dense spatial supervision. To measure the structure, we first use cluster analysis on the latent BEV grid on which d_{vector} operates (*i.e.*, B_{vector}). Class indices from the ground truth rasterized map are used as cluster labels for each of the latent vectors (*i.e.*, each BEV grid cells). The Silhouette score [30] is used to quantify cluster cohesion and separation for cluster quality evaluation and we use its mean of all data points:

$$S = \frac{1}{N} \sum_{i=1}^N \frac{b(i) - a(i)}{\max(a(i), b(i))}, \quad (6)$$

where $a(i)$ is the average distance between i and all other points in its cluster and $b(i)$ is the minimum average distance from i to the nearest cluster that i is not a part of.

Secondly, we leverage a dimensionality reduction technique that linearly transforms the high-dimensional latent space into a low-dimensional space that can be visualized and studied. Specifically, we perform a Principal Component Analysis (PCA) [9] on each scene’s latent features and analyze the top 3 components ordered by the amount of variance they capture from the data. We quantify the similarity between GT label and latent BEV grid for each scene by measuring the Mutual Information [32] between the ground truth (GT) raster map $\mathcal{M}_{\text{raster}}$ and the top 3 principal components of B_{vector} . Formally, given two sets of labels U and V , the Mutual Information is defined as :

$$MI(U, V) = \sum_{i=1}^{|U|} \sum_{j=1}^{|V|} \frac{|U_i \cap V_j|}{N} \log \left(\frac{N|U_i \cap V_j|}{|U_i||V_j|} \right). \quad (7)$$

In our case, U represents the flattened ground truth raster map after representing each pixel with a unique class index. Following common practice for mutual information estimation [12], we partition the continuous space of the PCA result into bins of finite size and choose 10 equidistant bins per dimension. V represents the flattened PCA result after binning and mapping each pixel to a unique index.

4. Experiments

4.1. Datasets and Evaluation Metrics

We conduct our experiments on nuScenes [1], which provides samples at 2Hz, and Argoverse2 [36], which we resample to 2Hz for consistency. We use images from the 6 (nuScenes) or 7 (Argoverse2) monocular cameras and corresponding ground truth vectorized map elements: road boundary (bound), lane dividers (div), and pedestrian crossings (ped). We use StreamMapNet’s [38] train and validation splits with no geospatial overlap for evaluation.

The performance on the vector map decoding task is evaluated for each of the three classes of polylines using Average Precision (AP) and combined with mean Average Precision (mAP). Following StreamMapNet, the AP thresholds are $\{0.5, 1.0, 1.5\}$ and $\{1.0, 1.5, 2.0\}$ for the $60\text{ m} \times 30\text{ m}$ and $100\text{ m} \times 50\text{ m}$ perception ranges, respectively. Intersection over Union (IoU) is evaluated per class for the raster map decoding task and reported as mean IoU (mIoU). The model runtime is evaluated in frames per second (FPS).

4.2. Implementation

StreamMapNet [38] serves as our implementation’s baseline with BEVFormer [15] as the learned BEV encoder e_{BEV} and temporal aggregation is done with a Gated Recurrent Unit (GRU) [4]. The vector map decoder d_{vector} is a custom deformable DETR decoder [42] that uses Multi-Point Attention [38].

The latent BEV grids have 256 channels at a resolution of 100×50 cells. We perform semantic segmentation on the three classes: lane dividers, road boundaries, and pedestrian crossings. Thus, $\hat{\mathcal{M}}_{\text{raster}} \in \mathbb{R}^{100 \times 50 \times 3}$. The decoder d_{raster} is a 4-layer CNN with output channels $\{128, 64, 32, 3\}$. The encoder e_{raster} is a 4-layer CNN with output channels $\{32, 64, 128, 256\}$. CNN1 and 2 both have 2 layers with input and output channel sizes of 256. All CNNs use convolutions with kernel size 3 and stride 1, batch normalization, and ReLU. With this configuration, AugMapNet has 52.70 million parameters, 6.3 % more than StreamMapNet. We train for 24 epochs with batch size 1. The model training is performed in parallel on 8 NVIDIA V100 GPUs. AdamW is used for optimization with a cosine annealing schedule and a 2×10^{-4} learning rate.

4.3. Baseline Models

We use several state-of-the-art models for vectorized map prediction as baselines: MapTR [19], SQD-MapNet [35], and StreamMapNet [38]. Additionally, we compare against hybrid methods that combine raster and vector representations: MapTRv2 [19], MapVR [39], and MGMap [20]. HIMap [41] and MapUnveiler [11] very recently surpassed StreamMapNet, but their code is not available yet, making direct comparisons under identical settings difficult. Most importantly, their contributions are orthogonal to ours, and our method can be applied to those architectures as well. For a fair and direct comparison, we ran all baselines ourselves on nuScenes under identical settings.

4.4. Quantitative Results

Tab. 1 shows the result of our AugMapNet model in comparison to relevant baseline models on the nuScenes dataset. StreamMapNet reaches 33.8 % mAP, other baselines are below. Naive auxiliary semantic segmentation (+Aux.) by adding d_{raster} optimized with $\mathcal{L}_{\text{raster}}$ gives a slight improvement with 34.0 % mAP. The results show that AugMapNet outperforms all baselines on each class-specific metric as well as on the overall mAP. Specifically, AugMapNet achieves 38.3 % mAP as compared to the best baseline, StreamMapNet, at 33.8 % mAP. This translates to 13.3 % relative improvement over the state-of-the-art StreamMapNet model. While the relative improvements on lane dividers (11.0 %) and road boundaries (5.6 %) are strong, the relative improvement introduced with AugMapNet on pedestrian crossings is immense (26.3 %). The FPS

Method	AP _{ped}	AP _{div}	AP _{bound}	mAP	FPS
MapTR [18]	7.5	23.0	35.8	22.1	16.0
MapVR [†] [39]	10.1	22.6	35.7	22.8	16.0
MGMMap [†] [20]	7.9	25.6	37.4	23.7	11.8
MapTRv2 [†] [19]	16.2	28.7	44.8	29.9	14.9
SQD-MapNet [35]	31.6	27.4	40.4	33.1	11.9
StreamMapNet [38]	31.2	27.3	42.9	33.8	13.2
StreamMapNet + Aux. [†]	31.9	27.7	42.3	34.0	13.2
AugMapNet [†] (ours)	39.4	30.3	45.3	38.3	11.9

Table 1. Performance of AugMapNet compared to various baselines at perception range $60\text{ m} \times 30\text{ m}$ on nuScenes split without geospatial overlap [38]. [†] denotes hybrid architectures. Aux. is auxiliary segmentation (described in Section 4.4).

Method	AP _{ped}	AP _{div}	AP _{bound}	mAP	FPS
VectorMapNet [21]	35.6	34.9	37.8	36.1	5.5
MapTR [18]	48.1	50.4	55.0	51.1	18.0
StreamMapNet [38]	56.0	54.4	61.0	57.1	14.2
AugMapNet (ours)	57.4	57.4	61.6	58.8	12.8

Table 2. Performance on Argoverse2. Baseline results from [38].

of AugMapNet differs only slightly from StreamMapNet with a relative change of -9.6% . The model size also remains almost the same at 1.8 GB for both StreamMapNet and AugMapNet. During training with batch size 1, we observe ~ 7.7 GB VRAM usage, a 1.6% increase over StreamMapNet.

Tab. 3 shows results on a larger perception range and applying our method to a different model. Beyond the reported 13.3% improvement on $60\text{ m} \times 30\text{ m}$, we get 24.8% on $100\text{ m} \times 50\text{ m}$. We provide further ablation on perception ranges in Supplementary A, showing an increase in relative improvement at larger perception ranges. To verify generalizability of our method, we apply our proposed latent BEV augmentation method to another model, SQD-MapNet [35], and denote it as “AugSQD.” The improvement is 15.4% on perception range $60\text{ m} \times 30\text{ m}$ and 34.4% on $100\text{ m} \times 50\text{ m}$.

To confirm our findings, we extend the evaluation to the Argoverse2 dataset [36]. Tab. 2 shows the result of our AugMapNet model in comparison to relevant baseline models. Again, AugMapNet outperforms all other approaches and reaches 58.8% mAP, a significant improvement over StreamMapNet.

4.5. Qualitative Results

Fig. 3 shows qualitative results of StreamMapNet and AugMapNet on a traffic scene from the nuScenes dataset. Both models correctly predict the lane dividers and road boundaries on the road that the autonomous vehicle drives on. AugMapNet detects the crosswalk in front of the autonomous vehicle that is missed by StreamMapNet, which exemplifies our large gains on pedestrian crossings. More examples can be found in the Supplementary D.

Range	Variant	AP _{ped}	AP _{div}	AP _{bound}	mAP	Impr.
$60\text{ m} \times 30\text{ m}^\ddagger$	StreamMapNet [38]	31.2	27.3	42.9	33.8	
	AugMapNet (ours)	39.4	30.3	45.3	38.3	13.3%
$100\text{ m} \times 50\text{ m}^*$	StreamMapNet [38]	25.5	19.3	24.7	23.2	
	AugMapNet (ours)	35.5	22.8	28.4	28.9	24.8%
$60\text{ m} \times 30\text{ m}^\ddagger$	SQD-MapNet [35]	31.6	27.4	40.4	33.1	
	AugSQD (ours)	38.5	30.2	45.8	38.2	15.4%
$100\text{ m} \times 50\text{ m}^*$	SQD-MapNet [35]	24.8	18.8	23.7	22.4	
	AugSQD (ours)	35.0	23.4	31.9	30.1	34.4%

Table 3. Range ablation on AugMapNet and application of our method to SQD-MapNet [35] giving “AugSQD”. Results on nuScenes [1]. AP thresholds ‡ : $\{0.5, 1.0, 1.5\}$, * : $\{1.0, 1.5, 2.0\}$.

4.6. Results on Latent BEV Grid Analysis

We compare the latent BEV grid features of StreamMapNet and AugMapNet with respect to: 1) cluster analysis, 2) similarity to GT label, 3) variance. First, we use cluster analysis on the latent BEV grid input to d_{vector} (i.e., B_{vector} in AugMapNet) to verify our hypothesis that latent BEV grid augmentation increases structure of the latent BEV grid. For scene 2 in Fig. 4, StreamMapNet reaches a Silhouette score of 0.086 vs. 0.119 for AugMapNet. Over the full nuScenes val dataset, the mean Silhouette score for AugMapNet is 4.5 times higher than StreamMapNet (0.076 vs. 0.017). Therefore, features from the BEV grid of the same class are better clustered in the latent space of AugMapNet compared to StreamMapNet, which could benefit classification. Since the ground truth labels have spatial structure, feature consistency among neighboring cells will also give a more consistent signal to the decoder.

Secondly, to assess the similarity between GT label and latent BEV grid, we visualize the PCA results for StreamMapNet and AugMapNet on two nuScenes data points in Fig. 4 (more results are in Supplementary E). The PCA result of the latent space shows spatial similarity with both the vectorized and rasterized map ground truths. Areas like background and drivable roads are well segmented and retrievable from the principal components. In both cases, the similarity appears higher for AugMapNet than for StreamMapNet, which matches the cluster analysis results. We can also see that the AugMapNet results have sharper boundaries that align well with the GT. To quantify the similarity, we compare Mutual Information (MI) values. In scene 2 in Fig. 4, StreamMapNet has an MI of 0.721, while AugMapNet has 0.761 ($+5.5\%$), which aligns with higher visual similarity. For the whole nuScenes dataset, the latent BEV grid of StreamMapNet has an MI of 0.61 ± 0.09 , while AugMapNet has 0.64 ± 0.09 ($+4.9\%$). To show that higher similarity is related to improved vector map prediction performance, we plot the mAP over MI for all nuScenes val data points in Fig. 5a (note: data points with 0.67 mAP are mostly scenes where the model predicts non-existing crosswalks). We measure a positive linear correlation between

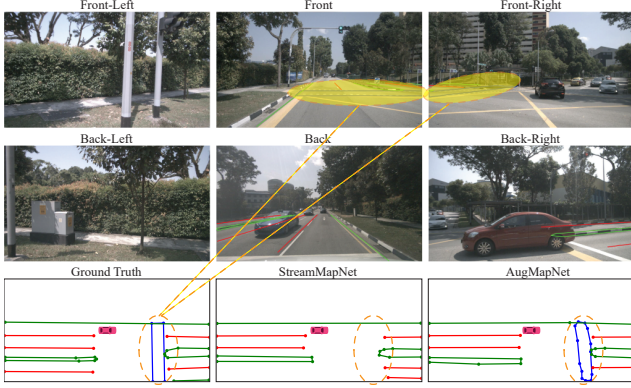


Figure 3. Qualitative result on nuScenes dataset. Input camera images (U) are at the top. Ground truth labels ($\mathcal{M}_{\text{vector}}$) and predicted vectorized maps ($\hat{\mathcal{M}}_{\text{vector}}$) are at the bottom. The orange circle highlights the crosswalk missed by StreamMapNet.

MI and vector map prediction performance, with $R^2 = 0.12$ for StreamMapNet and $R^2 = 0.22$ for AugMapNet. To determine whether AugMapNet’s increase of MI is statistically significant, we conduct a one-tailed t-test at a significance level $\alpha = 0.01$. The test yields $p \ll 0.001$, thus, we reject the null hypothesis and conclude that MI is significantly higher in AugMapNet. This result, in combination with the observed positive correlation between MI and vector map prediction performance, gives an interpretable insight and intuitive understanding of the performance improvement of AugMapNet over StreamMapNet.

Thirdly, a more structured latent BEV grid is expected to have an effect on its variance. We calculate the spatial variance of each channel in the latent BEV grids and take an average across all channels. For example, in scene 2 in Fig. 4, the variance of StreamMapNet latent space is 0.103 vs. 0.068 for AugMapNet. Results on the full nuScenes val dataset indicate that the latent space of AugMapNet indeed has a significantly lower variance compared to StreamMapNet, with an average latent BEV grid variance of 0.055 ± 0.006 for AugMapNet vs. 0.087 ± 0.008 for StreamMapNet.

We assume the variance reduction is caused by the BEV augmentation in AugMapNet. The raster map predicted in the BEV augmentation branch only carries low-dimensional class information due to the gradient stop from e_{raster} to $\mathcal{M}_{\text{raster}}$. Mapping this low-dimensional signal into the high-dimensional BEV grid latent space is expected to have a governing effect and reduce spatial variance.

An analysis of the relation between spatial variance of the latent BEV grid and vector map prediction performance is shown in Fig. 5b. In StreamMapNet, the variance does not correlate with prediction performance ($R^2 = 0.002$). In contrast, AugMapNet shows a positive correlation ($R^2 = 0.143$), suggesting that its spatial variance is explained by relevant, task-specific features.

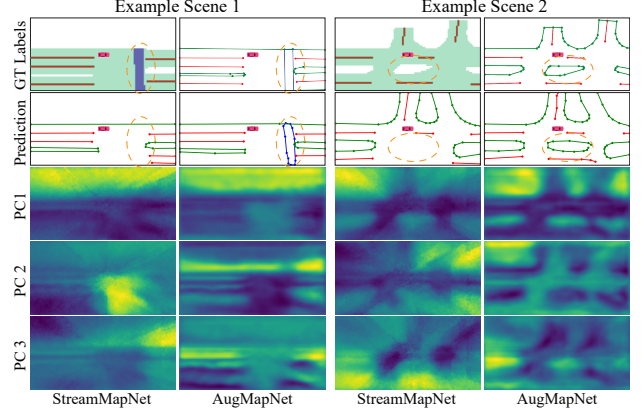


Figure 4. Rendering of ground truths $\mathcal{M}_{\text{raster}}$ and $\mathcal{M}_{\text{vector}}$, prediction $\hat{\mathcal{M}}_{\text{vector}}$, and the top 3 principal components of the latent BEV grid input to d_{vector} for StreamMapNet and AugMapNet (PC1-3). The orange circle highlights the crosswalk and traffic island missed by StreamMapNet.

4.7. Ablation of Latent BEV Grid Augmentation

We evaluate our proposed latent BEV grid augmentation method and compare different variants of gradient stopping to verify our final design. To allow a direct comparison with StreamMapNet, we do not include the additional processing CNNs (*i.e.*, CNN1 and CNN2 in Fig. 2). The results on the nuScenes dataset are shown in Tab. 4. The baseline is StreamMapNet with 33.8 % mAP. First, we run an Oracle experiment to determine the upper bound of our proposed BEV augmentation mechanism. Here the GT raster map, $\mathcal{M}_{\text{raster}}$, not the predicted raster map, $\hat{\mathcal{M}}_{\text{raster}}$, is passed to e_{raster} , hence the IoU scores are all 100.0 %. The result of the vector map decoding is 91.4 % mAP, confirming our hypothesis that augmenting the BEV grid with a rasterized map representation has the potential to drastically improve the vector map decoding.

The BEV augmentation mechanism introduces d_{raster} to decode $\hat{\mathcal{M}}_{\text{raster}}$ from B_{enc} and e_{raster} to encode it to B_{raster} . With no gradient stopping (“Full backprop”), it gives a small improvement with 34.8 % mAP. This variant also does raster map decoding well with 41.4 % mIoU.

Stopping the backpropagation between d_{raster} and e_{BEV} (“ d_{raster} grad stop”) slightly drops vector map decoding performance to 33.5 % mAP. This is expected, since d_{raster} is optimized by both $\mathcal{L}_{\text{vector}}$ and $\mathcal{L}_{\text{raster}}$, but has no influence on its input B_{enc} . As a result, a high-frequency latent space is likely formed by backpropagation. A comparison with the “Isolated” case (see below) shows that this hurts performance. Surprisingly, the raster map decoder still achieves 27.3 % mIoU from a latent BEV grid that was only optimized for the vector map decoding task. This finding suggests that decoding raster and vector representations requires similar latent features and shares synergies.

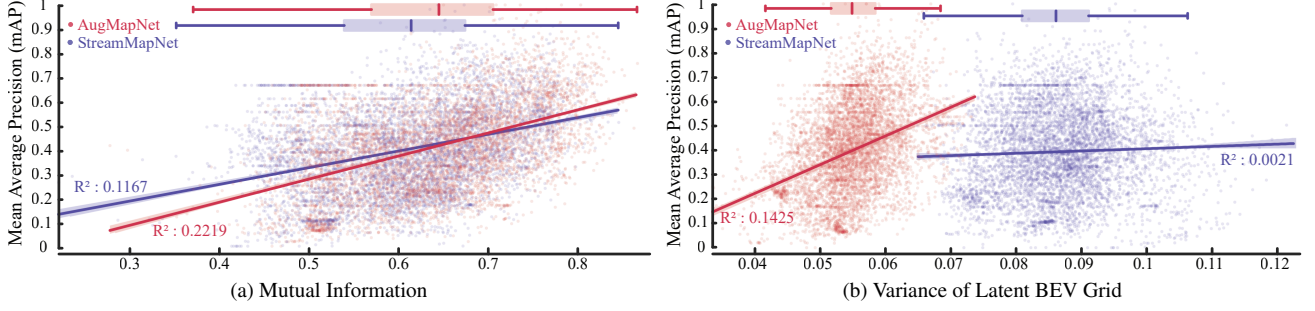


Figure 5. Vectorized map prediction performance versus (a) Mutual Information between top 3 principal components and ground truth raster map and (b) Variance of latent BEV grid for all nuScenes val data points. (StreamMapNet: blue, AugMapNet: red)

Variant	∇d	∇e	AP _{ped}	AP _{div}	AP _{bound}	mAP	mIoU
Baseline	-	-	32.4	28.8	42.5	33.8	-
Oracle	-	-	88.4	96.6	89.0	91.4	100.0
Full backprop	✓	✓	32.9	29.3	42.3	34.8	41.4
d_{raster} grad stop	✓	✓	30.8	28.1	41.5	33.5	27.3
e_{raster} grad stop	✓	✗	33.3	29.1	42.7	35.0	43.6
Isolated	✗	✗	33.9	29.9	42.7	35.5	28.5

Table 4. Ablation of BEV augmentation on nuScenes. Oracle uses GT, $\mathcal{M}_{\text{raster}}$, for augmentation. ∇ indicates whether gradients are backpropagated from either d_{raster} or e_{raster} (*i.e.*, dashed lines in Fig. 2). AP and mIoU evaluate $\hat{\mathcal{M}}_{\text{vector}}$ and $\hat{\mathcal{M}}_{\text{raster}}$, respectively.

Alternatively, stopping the backpropagation from e_{raster} to d_{raster} (“ e_{raster} grad stop”) improves performance to 35.0 % mAP with 43.6 % mIoU. Finally, stopping backpropagation at both locations (“Isolated”) achieves the best result with 35.5 % mAP. “Isolated” is used in AugMapNet, since it cuts off the rasterized map branch from the rest of the model. Specifically, the latent BEV grid before augmentation, B_{align} , is unaffected by the segmentation loss and can purely optimize for vector map decoding. $\hat{\mathcal{M}}_{\text{raster}}$ is learned separately and augments the latent BEV grid to improve the features for vector map decoding.

4.8. Ablation of Latent BEV Grid Processing

This study, shown in Tab. 5, compares different variants for additional processing between the encoder and decoder. Here we do not use our BEV augmentation to allow direct comparison with the StreamMapNet baseline, thus there is only one CNN (*i.e.*, CNN1 in Fig. 2). Comparing StreamMapNet (a) with index b shows that we get a significant improvement of 6.8 % mAP just from adding a single convolution layer. We investigate the effect of kernel size by comparing 1, 3, and 5 (b, c, d, resp.). Size 3 is used for further experiments since it gives the best result with 36.7 % mAP. Adding a layer (e) gives a slight improvement, but further layers show a performance plateau (f, g). Thus we choose 2 CNN layers with kernel size 3 (e) for AugMapNet.

Index	Kernel	# Layers	AP _{ped}	AP _{div}	AP _{bound}	mAP
a)	-	0	31.2	27.3	42.9	33.8
b)	1	1	36.6	30.3	41.4	36.1
c)	3	1	36.4	30.0	43.7	36.7
d)	5	1	33.9	30.3	43.8	36.0
e)	3	2	38.9	29.6	43.5	37.3
f)	3	3	36.7	30.0	43.1	36.6
g)	3	4	34.3	30.0	44.8	36.4

Table 5. Ablation of BEV processing parameters of an extra CNN. a) is StreamMapNet [38] and e) is AugMapNet’s setting.

5. Conclusion

We presented AugMapNet, a novel method for online vectorized HD map construction from multiple camera views. It enhances the latent BEV grid by injecting spatial features from a predicted raster map, providing better dense spatial supervision to the vector decoder than other hybrid architectures, while being as easy to integrate and as generic as auxiliary supervision. Experiments on nuScenes and Argoverse2 show an improvement in mAP of up to 13.3 % over the StreamMapNet baseline with minimal parameter overhead. AugMapNet shows particular strength in detecting complex map characteristics, such as pedestrian crossings, with a substantial 26.3 % relative performance gain. Its relative improvements are even higher on larger perception ranges. While impressive, these findings show that our BEV augmentation method still has untapped potential when compared to our Oracle results.

Additionally, our analysis of the latent BEV grid reveals that AugMapNet forms a more structured and task-relevant feature space. Mutual Information analysis shows that AugMapNet’s augmented BEV grid has much higher similarity with the ground truth raster map, which is correlated with improved vector map predictions, validating our hypothesis. Improvements in cluster quality and variance of the latent space further support our reasoning.

In conclusion, AugMapNet highlights the importance of dense spatial supervision in BEV-based vector map construction and opens a new paradigm for further research on the synergy between raster and vector representations.

References

- [1] Holger Caesar, Varun Bankiti, Alex H Lang, Sourabh Vora, Venice Erin Liong, Qiang Xu, Anush Krishnan, Yu Pan, Giancarlo Baldan, and Oscar Beijbom. nuscenes: A multi-modal dataset for autonomous driving. In *Proceedings of the IEEE/CVF conference on computer vision and pattern recognition*, pages 11621–11631, 2020. 5, 6, 1
- [2] Yigit Baran Can, Alexander Liniger, Danda Pani Paudel, and Luc Van Gool. Structured bird’s-eye-view traffic scene understanding from onboard images. In *Proceedings of the IEEE/CVF International Conference on Computer Vision*, pages 15661–15670, 2021. 2
- [3] Xiaowei Chi, Jiaming Liu, Ming Lu, Rongyu Zhang, Zhaoqing Wang, Yandong Guo, and Shanghang Zhang. Bev-san: Accurate bev 3d object detection via slice attention networks. In *Proceedings of the IEEE/CVF Conference on Computer Vision and Pattern Recognition*, pages 17461–17470, 2023. 3
- [4] Kyunghyun Cho, Bart van Merriënboer, Caglar Gulcehre, Dzmitry Bahdanau, Fethi Bougares, Holger Schwenk, and Yoshua Bengio. Learning phrase representations using RNN encoder–decoder for statistical machine translation. In *Proceedings of the 2014 Conference on Empirical Methods in Natural Language Processing (EMNLP)*, pages 1724–1734, Doha, Qatar, 2014. Association for Computational Linguistics. 5
- [5] Casey Chu, Andrey Zhmoginov, and Mark Sandler. CycleGAN, a master of steganography. In *Machine Deception Workshop at NeurIPS*, 2017. 3, 4
- [6] Wenjie Ding, Limeng Qiao, Xi Qiu, and Chi Zhang. Pivotnet: Vectorized pivot learning for end-to-end hd map construction. In *Proceedings of the IEEE/CVF International Conference on Computer Vision*, pages 3672–3682, 2023. 2, 3
- [7] Jiyang Gao, Chen Sun, Hang Zhao, Yi Shen, Dragomir Anguelov, Congcong Li, and Cordelia Schmid. Vectornet: Encoding hd maps and agent dynamics from vectorized representation. In *Proceedings of the IEEE/CVF conference on computer vision and pattern recognition*, pages 11525–11533, 2020. 1
- [8] Chunrui Han, Jinrong Yang, Jianjian Sun, Zheng Ge, Runpei Dong, Hongyu Zhou, Weixin Mao, Yuang Peng, and Xiangyu Zhang. Exploring recurrent long-term temporal fusion for multi-view 3d perception. *IEEE Robotics and Automation Letters*, 2024. 2
- [9] Harold Hotelling. Analysis of a complex of statistical variables into principal components. *Journal of educational psychology*, 24(6):417, 1933. 3, 5
- [10] Junjie Huang and Guan Huang. Bevdet4d: Exploit temporal cues in multi-camera 3d object detection. *arXiv preprint arXiv:2203.17054*, 2022. 2
- [11] Nayeon Kim, Hongje Seong, Daehyun Ji, and Sujin Jang. Unveiling the hidden: Online vectorized hd map construction with clip-level token interaction and propagation. In *NeurIPS*, 2024. 5
- [12] Alexander Kraskov, Harald Stögbauer, and Peter Grassberger. Estimating mutual information. *Physical Review E—Statistical, Nonlinear, and Soft Matter Physics*, 69(6): 066138, 2004. 5
- [13] Abhinav Kumar, Yuliang Guo, Xinyu Huang, Liu Ren, and Xiaoming Liu. Seabird: Segmentation in bird’s view with dice loss improves monocular 3d detection of large objects. In *Proceedings of the IEEE/CVF Conference on Computer Vision and Pattern Recognition*, pages 10269–10280, 2024. 2, 3
- [14] Qi Li, Yue Wang, Yilun Wang, and Hang Zhao. Hdmapnet: An online hd map construction and evaluation framework. In *2022 International Conference on Robotics and Automation (ICRA)*, pages 4628–4634. IEEE, 2022. 1, 2, 3
- [15] Zhiqi Li, Wenhai Wang, Hongyang Li, Enze Xie, Chonghao Sima, Tong Lu, Yu Qiao, and Jifeng Dai. Bevformer: Learning bird’s-eye-view representation from multi-camera images via spatiotemporal transformers. In *European conference on computer vision*, pages 1–18. Springer, 2022. 1, 2, 5
- [16] Zhiqi Li, Zhiding Yu, Wenhai Wang, Anima Anandkumar, Tong Lu, and Jose M Alvarez. Fb-bev: Bev representation from forward-backward view transformations. In *Proceedings of the IEEE/CVF International Conference on Computer Vision*, pages 6919–6928, 2023. 3
- [17] Zhidong Liang, Ming Zhang, Zehan Zhang, Xian Zhao, and Shiliang Pu. Rangercnn: Towards fast and accurate 3d object detection with range image representation. *arXiv preprint arXiv:2009.00206*, 2020. 3
- [18] Bencheng Liao, Shaoyu Chen, Xinggang Wang, Tianheng Cheng, Qian Zhang, Wenyu Liu, and Chang Huang. Maptr: Structured modeling and learning for online vectorized hd map construction. In *International Conference on Learning Representations*, 2023. 6
- [19] Bencheng Liao, Shaoyu Chen, Yunchi Zhang, Bo Jiang, Qian Zhang, Wenyu Liu, Chang Huang, and Xinggang Wang. Maptrv2: An end-to-end framework for online vectorized hd map construction. *International Journal of Computer Vision*, 2025. 1, 2, 3, 5, 6
- [20] Xiaolu Liu, Song Wang, Wentong Li, Ruizi Yang, Junbo Chen, and Jianke Zhu. Mgmmap: Mask-guided learning for online vectorized hd map construction. In *Proceedings of the IEEE/CVF Conference on Computer Vision and Pattern Recognition*, pages 14812–14821, 2024. 3, 4, 5, 6
- [21] Yicheng Liu, Tianyuan Yuan, Yue Wang, Yilun Wang, and Hang Zhao. Vectormapnet: End-to-end vectorized hd map learning. In *International Conference on Machine Learning*, pages 22352–22369. PMLR, 2023. 1, 2, 3, 6
- [22] Leland McInnes, John Healy, and James Melville. Umap: Uniform manifold approximation and projection for dimension reduction. *arXiv preprint arXiv:1802.03426*, 2018. 3
- [23] Lu Mi, Hang Zhao, Charlie Nash, Xiaohan Jin, Jiyang Gao, Chen Sun, Cordelia Schmid, Nir Shavit, Yuning Chai, and Dragomir Anguelov. Hdmapgen: A hierarchical graph generative model of high definition maps. In *Proceedings of the IEEE/CVF Conference on Computer Vision and Pattern Recognition*, pages 4227–4236, 2021. 2
- [24] Fausto Milletari, Nassir Navab, and Seyed-Ahmad Ahmadi. V-net: Fully convolutional neural networks for volumetric

- medical image segmentation. In *2016 Fourth International Conference on 3D Vision (3DV)*, pages 565–571. Ieee, 2016. 4, 2
- [25] Thomas Monninger, Vandana Dokkadi, Md Zafar Anwar, and Steffen Staab. TempBEV: Improving learned bev encoders with combined image and bev space temporal aggregation. In *2024 IEEE/RSJ International Conference on Intelligent Robots and Systems (IROS)*, pages 9668–9675. IEEE, 2024. 2
- [26] Bowen Pan, Jiankai Sun, Ho Yin Tiga Leung, Alex Andonian, and Bolei Zhou. Cross-view semantic segmentation for sensing surroundings. *IEEE Robotics and Automation Letters*, 5(3):4867–4873, 2020. 1
- [27] Jinhyung Park, Chenfeng Xu, Shijia Yang, Kurt Keutzer, Kris Kitani, Masayoshi Tomizuka, and Wei Zhan. Time will tell: New outlooks and a baseline for temporal multi-view 3d object detection. In *International Conference on Learning Representations*, 2023. 2
- [28] Marc Perez, Antonio Agudo, Gijs Dubbelman, and Pavol Jancura. Class prototypical loss for enhanced feature separation in 3d object detection. In *ITSC*, 2024. 3
- [29] Jonah Philion and Sanja Fidler. Lift, splat, shoot: Encoding images from arbitrary camera rigs by implicitly unprojecting to 3d. In *Computer Vision–ECCV 2020: 16th European Conference, Glasgow, UK, August 23–28, 2020, Proceedings, Part XIV 16*, pages 194–210. Springer, 2020. 1, 2
- [30] Peter J Rousseeuw. Silhouettes: a graphical aid to the interpretation and validation of cluster analysis. *Journal of computational and applied mathematics*, 20:53–65, 1987. 3, 4
- [31] Cristiano Saltori, Aljosa Osep, Elisa Ricci, and Laura Leal-Taixé. Walking your lidog: A journey through multiple domains for lidar semantic segmentation. In *Proceedings of the IEEE/CVF International Conference on Computer Vision*, pages 196–206, 2023. 3
- [32] Claude Elwood Shannon. A mathematical theory of communication. *The Bell system technical journal*, 27(3):379–423, 1948. 5
- [33] Laurens Van der Maaten and Geoffrey Hinton. Visualizing data using t-sne. *Journal of machine learning research*, 9(11), 2008. 3
- [34] Shihao Wang, Yingfei Liu, Tiancai Wang, Ying Li, and Xiangyu Zhang. Exploring object-centric temporal modeling for efficient multi-view 3d object detection. In *Proceedings of the IEEE/CVF International Conference on Computer Vision*, pages 3621–3631, 2023. 2
- [35] Shuo Wang, Fan Jia, Weixin Mao, Yingfei Liu, Yucheng Zhao, Zehui Chen, Tiancai Wang, Chi Zhang, Xiangyu Zhang, and Feng Zhao. Stream query denoising for vectorized hd-map construction. In *European Conference on Computer Vision*, pages 203–220. Springer, 2024. 5, 6
- [36] Benjamin Wilson, William Qi, Tanmay Agarwal, John Lambert, Jagjeet Singh, Siddhesh Khandelwal, Bowen Pan, Ratnesh Kumar, Andrew Hartnett, Jhony Kaesemodel Pontes, et al. Argoverse 2: Next generation datasets for self-driving perception and forecasting. *arXiv preprint arXiv:2301.00493*, 2023. 5, 6
- [37] Chenyu Yang, Yuntao Chen, Hao Tian, Chenxin Tao, Xizhou Zhu, Zhaoxiang Zhang, Gao Huang, Hongyang Li, Yu Qiao, Lewei Lu, et al. Bevformer v2: Adapting modern image backbones to bird’s-eye-view recognition via perspective supervision. In *Proceedings of the IEEE/CVF Conference on Computer Vision and Pattern Recognition*, pages 17830–17839, 2023. 2
- [38] Tianyuan Yuan, Yicheng Liu, Yue Wang, Yilun Wang, and Hang Zhao. Streammapnet: Streaming mapping network for vectorized online hd map construction. In *Proceedings of the IEEE/CVF Winter Conference on Applications of Computer Vision*, pages 7356–7365, 2024. 1, 2, 3, 4, 5, 6, 8
- [39] Gongjie Zhang, Jiahao Lin, Shuang Wu, Zhipeng Luo, Yang Xue, Shijian Lu, Zuoguan Wang, et al. Online map vectorization for autonomous driving: A rasterization perspective. *Advances in Neural Information Processing Systems*, 36, 2024. 2, 3, 5, 6
- [40] Jinqing Zhang, Yanan Zhang, Qingjie Liu, and Yunhong Wang. Sa-bev: Generating semantic-aware bird’s-eye-view feature for multi-view 3d object detection. In *Proceedings of the IEEE/CVF International Conference on Computer Vision*, pages 3348–3357, 2023. 3
- [41] Yi Zhou, Hui Zhang, Jiaqian Yu, Yifan Yang, Sangil Jung, Seung-In Park, and ByungIn Yoo. Himap: Hybrid representation learning for end-to-end vectorized hd map construction. In *Proceedings of the IEEE/CVF Conference on Computer Vision and Pattern Recognition*, pages 15396–15406, 2024. 3, 5
- [42] Xizhou Zhu, Weijie Su, Lewei Lu, Bin Li, Xiaogang Wang, and Jifeng Dai. Deformable detr: Deformable transformers for end-to-end object detection. In *International Conference on Learning Representations*, 2021. 2, 5
- [43] Jannik Zürn, Johan Vertens, and Wolfram Burgard. Lane graph estimation for scene understanding in urban driving. *IEEE Robotics and Automation Letters*, 6(4):8615–8622, 2021. 2

AugMapNet: Improving Spatial Latent Structure via BEV Grid Augmentation for Enhanced Vectorized Online HD Map Construction

Supplementary Material

Overview of Supplementary Material

The supplementary material includes the following parts:

- A. Ablation of Perception Ranges
- B. Formulation of Dense Spatial Supervision
- C. Mathematical Definition of Loss Functions
- D. Additional Qualitative Results
- E. Visualization of Principal Components

A. Ablation of Perception Ranges

Tab. 6 shows the results on various perception ranges. Beyond the reported 13.3 % improvement on perception range $60\text{ m} \times 30\text{ m}$, we get 19.6 % on $80\text{ m} \times 40\text{ m}$, 24.8 % on $100\text{ m} \times 50\text{ m}$, 23.4 % on $120\text{ m} \times 60\text{ m}$, and 41.4 % on $150\text{ m} \times 75\text{ m}$. We find that the relative improvement of AugMapNet increases with larger perception ranges, which suggests a stronger benefit of our augmentation method on wider ranges.

B. Formulation of Dense Spatial Supervision

The loss is calculated over all elements of the output representation $\hat{\mathcal{M}}$. Supervision is done by optimizing a learnable set of weights W based on the gradients of the loss:

$$\frac{\partial L}{\partial W} = \frac{\partial L}{\partial \hat{\mathcal{M}}} \frac{\partial \hat{\mathcal{M}}}{\partial W}. \quad (8)$$

The total amount of spatial supervision therefore is related to the number of elements in $\hat{\mathcal{M}}$.

In the case of a raster map decoder, the predicted output is a rasterized representation: $\hat{\mathcal{M}} = \hat{\mathcal{M}}_{\text{raster}}$. The total gradient signal is calculated from the loss over all pixels. For a raster with spatial resolution $H = 100$ and $W = 50$, this gives a spatial supervision for $|\hat{\mathcal{M}}_{\text{raster}}| = H \times W = 100 \times 50 = 5000$ elements.

In the case of a vector map decoder, the predicted output is a vectorized representation: $\hat{\mathcal{M}} = \hat{\mathcal{M}}_{\text{vector}}$. The total gradient signal is calculated from the loss over all points of all polylines. Our model outputs $N = 100$ polylines, with $N_p = 20$ points each, which gives spatial supervision for at most $|\hat{\mathcal{M}}_{\text{vector}}| = N \times N_p = 100 \times 20 = 2000$ elements. Note that, in DETR-style decoders, elements that are correctly predicted as empty class do not induce spatial supervision. Hence, this number is the upper bound and the actual supervision is typically even sparser.

We believe that this difference in the number of elements is why integrating dense spatial supervision into vectorized map decoding is so effective.

Range	Variant	AP _{ped}	AP _{div}	AP _{bound}	mAP	Impr.
$60\text{ m} \times 30\text{ m}^\ddagger$	StreamMapNet [38]	31.2	27.3	42.9	33.8	13.3 %
	AugMapNet (ours)	39.4	30.3	45.3	38.3	
$80\text{ m} \times 40\text{ m}^\ddagger$	StreamMapNet [38]	19.4	18.9	24.1	20.8	19.6 %
	AugMapNet (ours)	25.9	21.1	27.6	24.9	
$100\text{ m} \times 50\text{ m}^*$	StreamMapNet [38]	25.5	19.3	24.7	23.2	24.8 %
	AugMapNet (ours)	35.5	22.8	28.4	28.9	
$120\text{ m} \times 60\text{ m}^*$	StreamMapNet [38]	19.29	10.95	12.79	14.34	23.4 %
	AugMapNet (ours)	24.13	12.72	16.26	17.70	
$150\text{ m} \times 75\text{ m}^*$	StreamMapNet [38]	10.5	6.4	3.9	6.9	41.4 %
	AugMapNet (ours)	15.2	7.5	6.7	9.8	

Table 6. Range ablation on nuScenes dataset [1]. AP thresholds ‡ : {0.5, 1.0, 1.5}, * : {1.0, 1.5, 2.0}.

C. Mathematical Definition of Loss Functions

The formulation of the vector map decoder loss, $\mathcal{L}_{\text{vector}}$, is taken from StreamMapNet [38] and consists of multiple components. As the first step of the polyline matching loss, $\mathcal{L}_{\text{line}}$, bipartite matching is performed between predicted and GT polylines. After matching, the smooth L1 loss is calculated for each of the N_p points P_j of the matched polyline P . The best one in the permutation group, Γ , as introduced in MapTR [19], is used:

$$\mathcal{L}_{\text{line}}(\hat{P}, P) = \min_{\gamma \in \Gamma} \frac{1}{N_p} \sum_{j=1}^{N_p} \mathcal{L}_{\text{SmoothL1}}(\hat{P}_j, P_{\gamma(j)}). \quad (9)$$

The classification loss, $\mathcal{L}_{\text{class}}$, calculates the loss between the ground truth class vector, c , and predicted class vector, \hat{c} , for each polyline. The loss function is the Focal loss:

$$\mathcal{L}_{\text{class}}(\hat{c}, c) = \mathcal{L}_{\text{Focal}}(\hat{c}, c). \quad (10)$$

An auxiliary transformation loss, $\mathcal{L}_{\text{trans}}$, is used to match the ego-motion transformation in latent space. Given a standard 4×4 transformation matrix, T , between the coordinate frames of $t - 1$ and t , the polyline of the vector map at time t is expressed as $P = T \cdot \text{homogeneous}(P')_{:,0:2}$, where P' is the polyline of the vector map at time $t - 1$. For a query in the vector map decoder at time t , Q , an auxiliary prediction is made with $\hat{P}^{\text{aux}} = \text{Reg}(Q)$. The auxiliary transformation loss is then defined as:

$$\mathcal{L}_{\text{trans}}(\hat{P}^{\text{aux}}, P) = \sum_{j=1}^{N_p} \mathcal{L}_{\text{SmoothL1}}(\hat{P}_j^{\text{aux}}, P_j). \quad (11)$$

The final loss is a weighted sum of the above loss terms with the factors $\lambda_1 = 50.0$, $\lambda_2 = 5.0$, and $\lambda_3 = 0.1$ over all

predicted polylines in $\hat{\mathcal{M}}_{\text{vector}}$:

$$\mathcal{L}_{\text{vector}} = \sum_{P \in \hat{\mathcal{M}}_{\text{vector}}} (\lambda_1 \mathcal{L}_{\text{line}} + \lambda_2 \mathcal{L}_{\text{class}} + \lambda_3 \mathcal{L}_{\text{trans}}). \quad (12)$$

The raster map decoder loss $\mathcal{L}_{\text{raster}}$ is the Dice loss [24]:

$$\mathcal{L}_{\text{raster}}(\hat{\mathcal{M}}_{\text{seg}}, \mathcal{M}_{\text{seg}}) = \mathcal{L}_{\text{Dice}}(\hat{\mathcal{M}}_{\text{seg}}, \mathcal{M}_{\text{seg}}). \quad (13)$$

D. Additional Qualitative Results

We provide further qualitative results to highlight the benefits of AugMapNet.

A separate video file is included with this submission to show the performance of AugMapNet on a full scene. It overlays the predicted vector map polylines in each camera view to visualize the spatial accuracy.

Fig. 6 shows a scene where StreamMapNet misses the road divider on the left side of the ego vehicle. AugMapNet predicts the road divider to include a roadway turnout, which is reasonable given the large driveway that is occupied by a truck. Fig. 7 shows a scene where a traffic island and a crosswalk to the front-left of the ego vehicle are missed by StreamMapNet, but correctly predicted by AugMapNet. Fig. 8 visualizes a rainy scene to show model performance under challenging weather conditions, including a rain droplet on the front-facing camera lens that limits visibility. StreamMapNet misses a crosswalk in the area that AugMapNet predicts correctly. Fig. 9 shows a scene at night with limited illumination. AugMapNet predicts the left road boundary fairly accurately given the visibility, whereas StreamMapNet misses it completely.

E. Visualization of Principal Components

As an extension to the top 3 Principal Components (PCs) visualized in Fig. 4, we visualize the top 16 PCs for example scene 1 in Fig. 10 and for example scene 2 in Fig. 11. A general observation is that the PCs tend to have more radial artifacts in StreamMapNet. The PCs of AugMapNet have better spatial structure and correspondence with the GT map due to dense spatial supervision.

Finally, Fig. 12 gives more details on example scene 1, where StreamMapNet misses a pedestrian crossing that is correctly predicted by AugMapNet. Specifically, we highlight the PC that has the highest visual correspondence to the pedestrian crossing GT out of the top 16 PCs visualized in Fig. 10 for each StreamMapNet and AugMapNet. It is PC 14 for StreamMapNet and PC 8 for AugMapNet. The smaller number for AugMapNet indicates that AugMapNet has stronger latent features for pedestrian crossings, which likely helped with its correct prediction. This also matches the better visual correspondence between the AugMapNet PC and the pedestrian crossing GT compared to StreamMapNet.

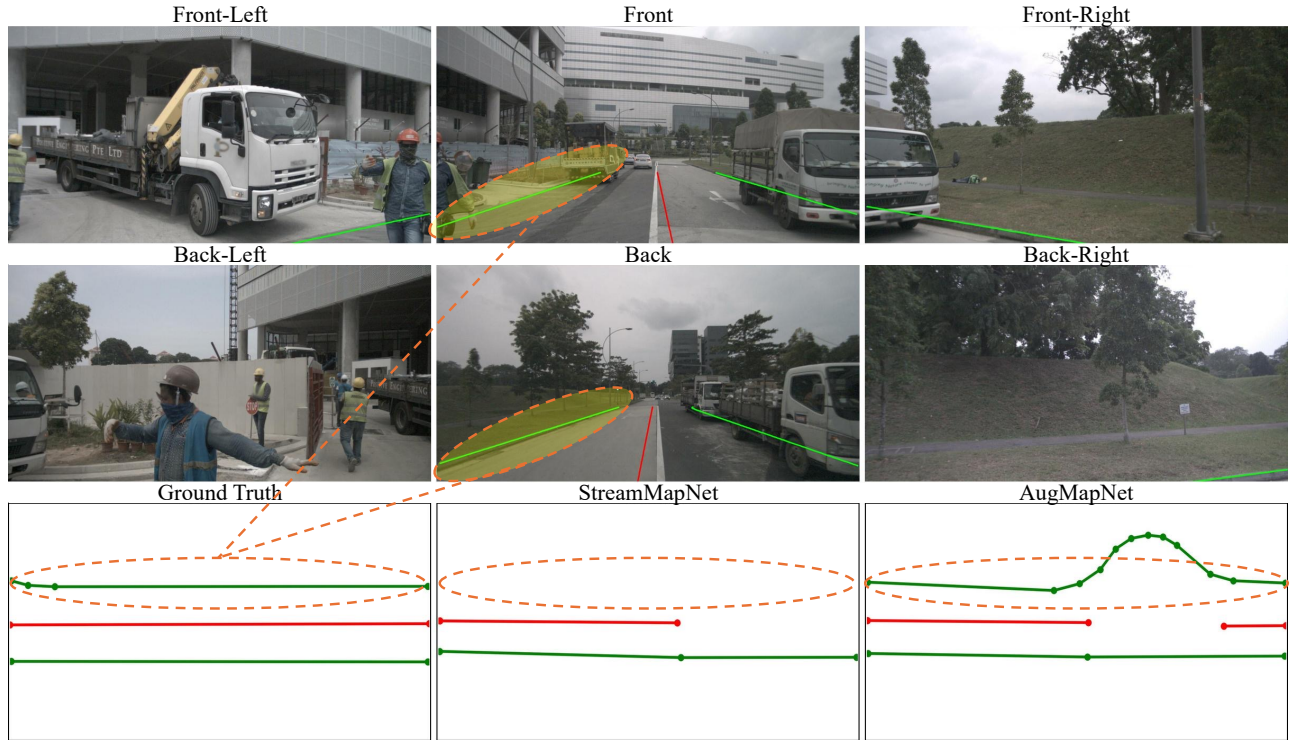


Figure 6. Qualitative results for example scene 3 with an extensive driveway on the left side. Lane dividers are red, road boundaries are green, and pedestrian crossings are blue.

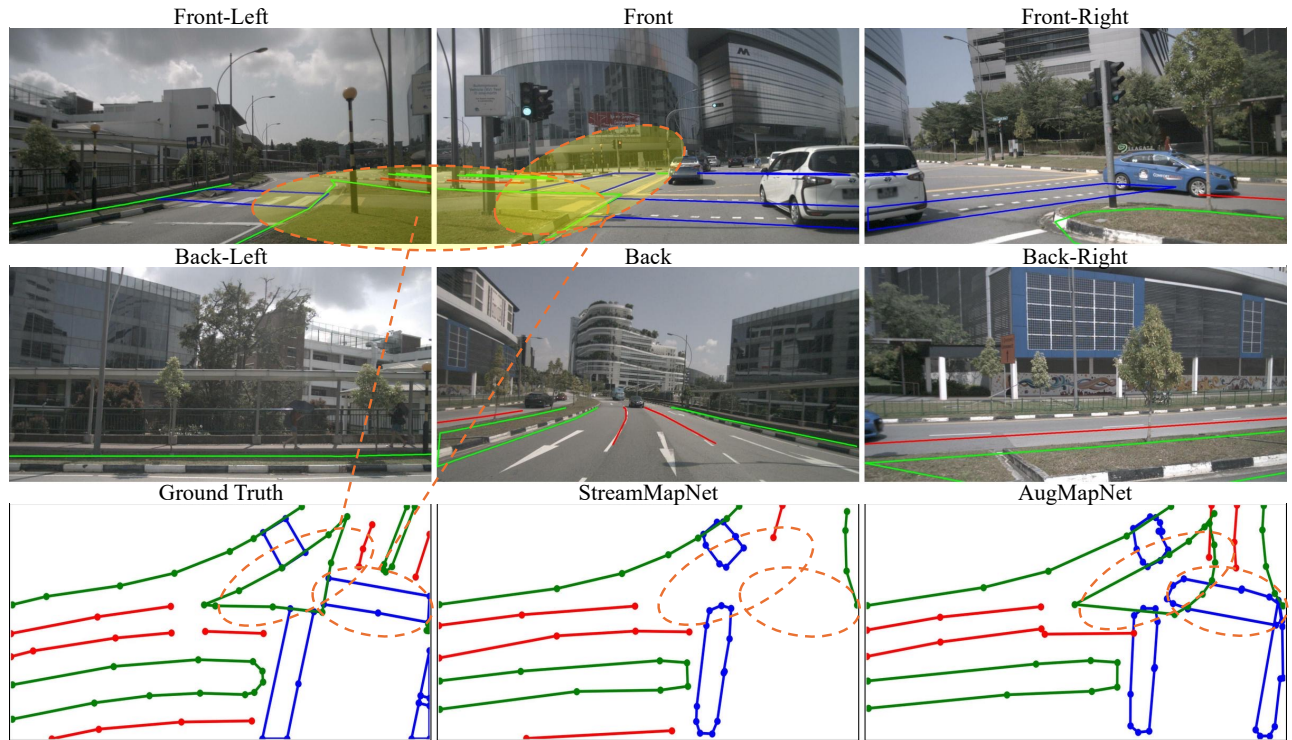


Figure 7. Qualitative results for example scene 4 with traffic island and pedestrian crossing on the left. Lane dividers are red, road boundaries are green, and pedestrian crossings are blue.

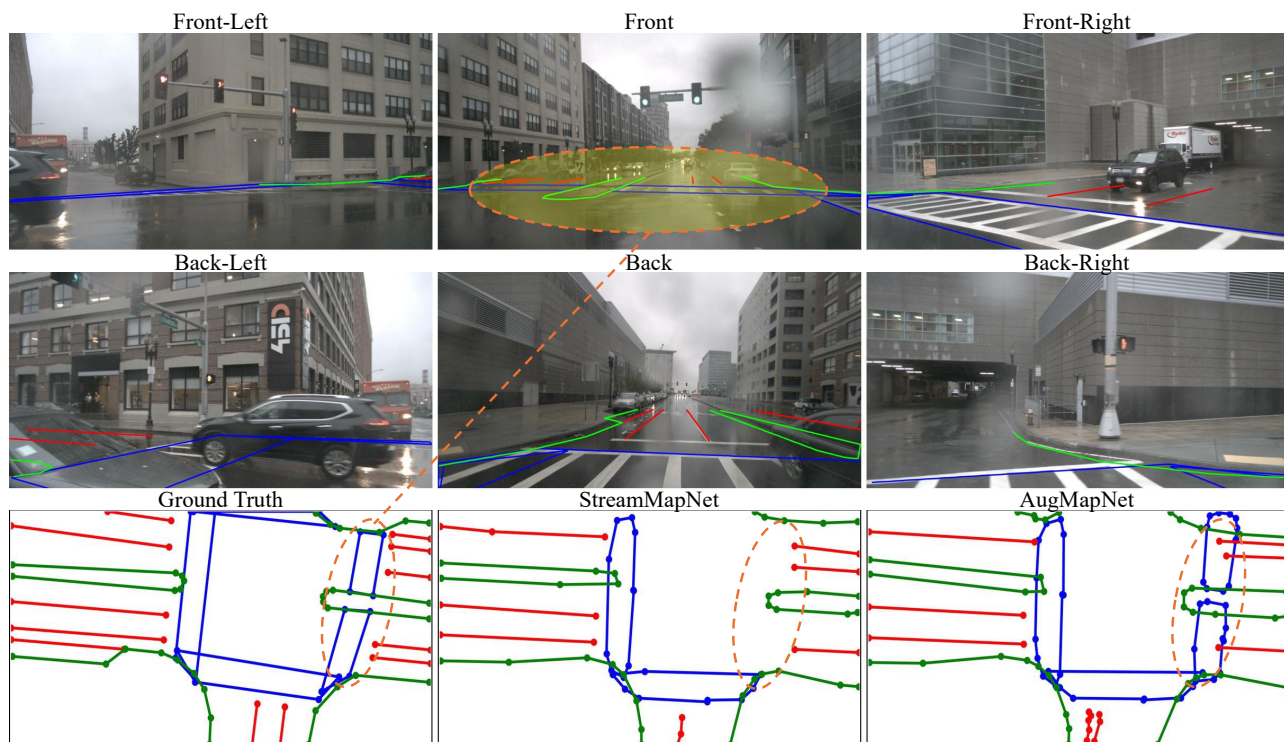


Figure 8. Qualitative results for example scene 5 under rainy conditions. Lane dividers are red, road boundaries are green, and pedestrian crossings are blue.

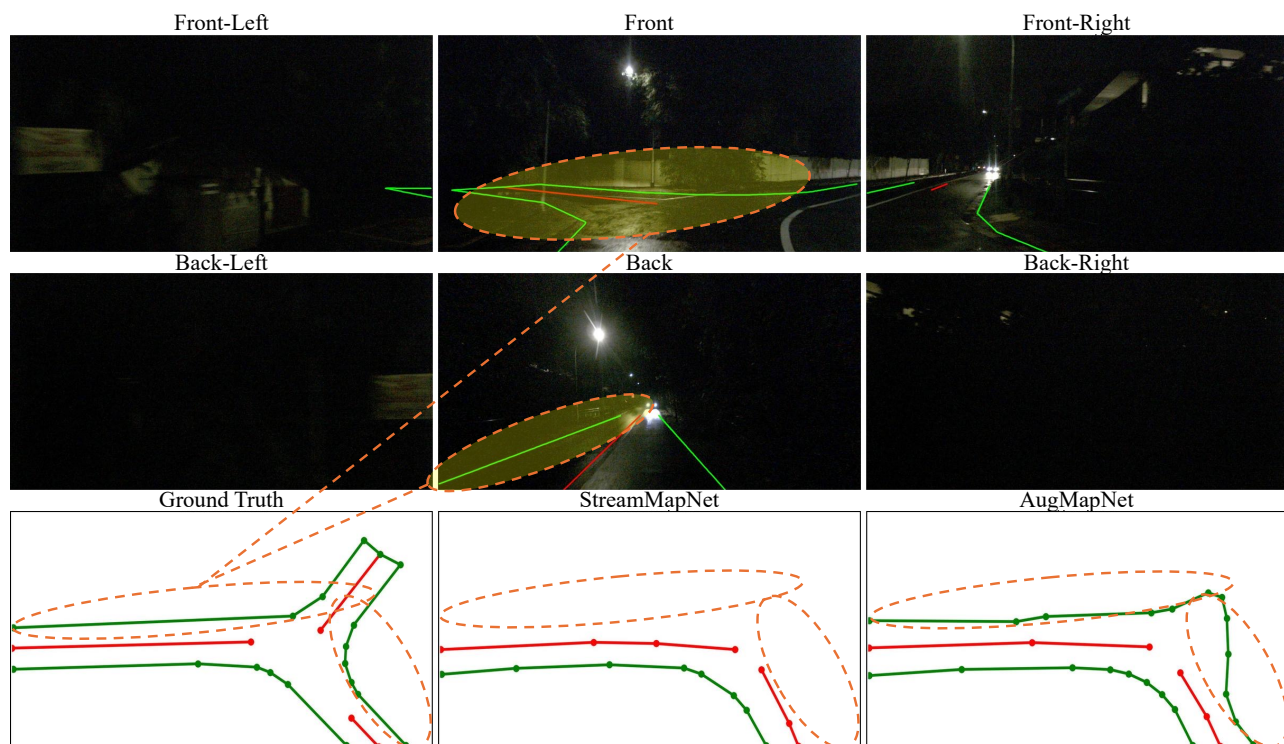
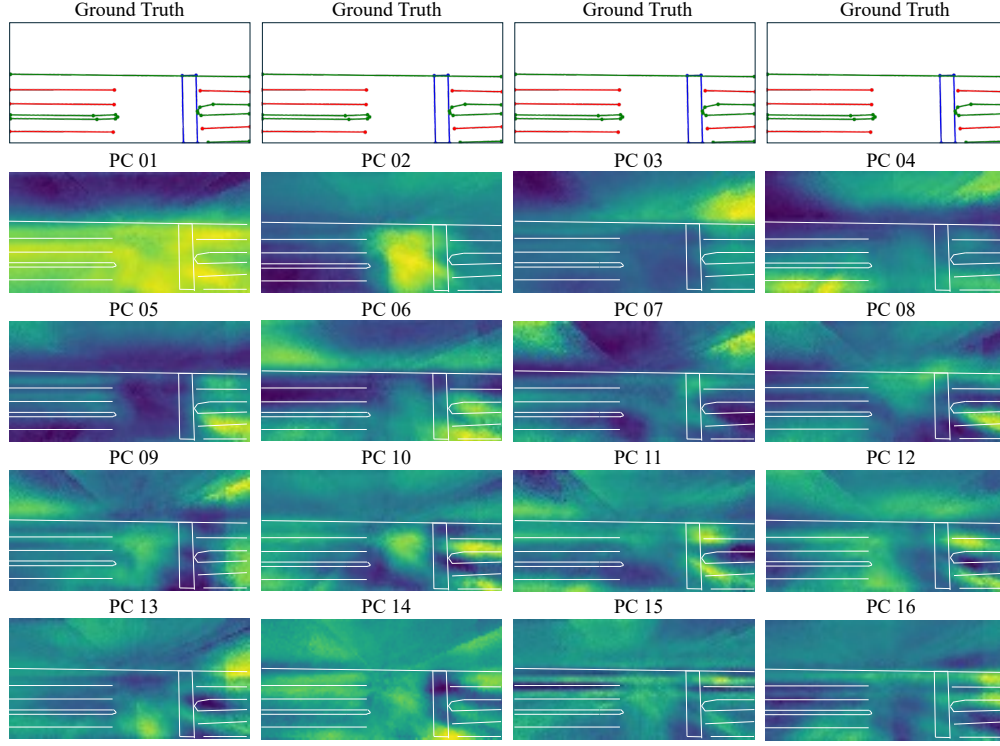
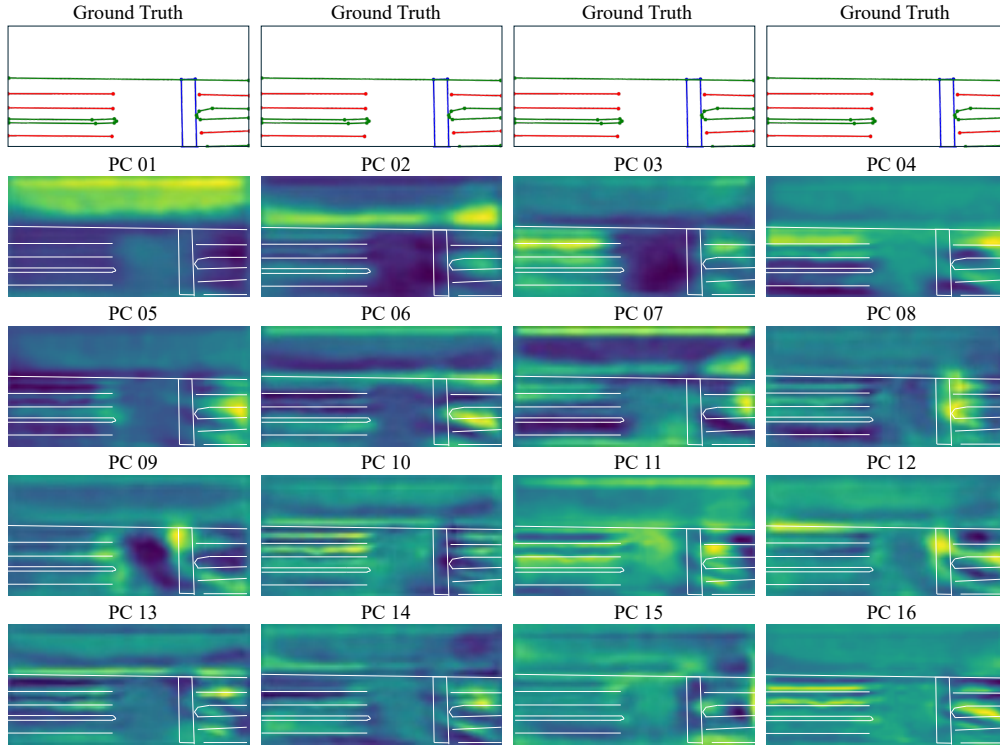


Figure 9. Qualitative results for example scene 6 with limited illumination. Lane dividers are red, road boundaries are green, and pedestrian crossings are blue.

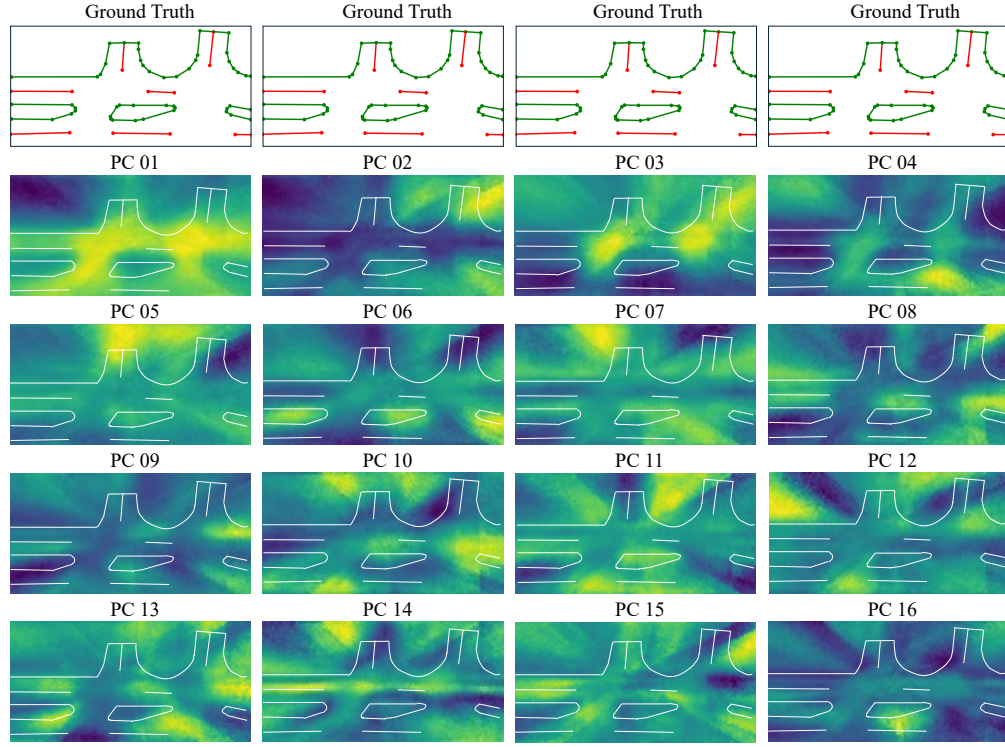


(a) StreamMapNet

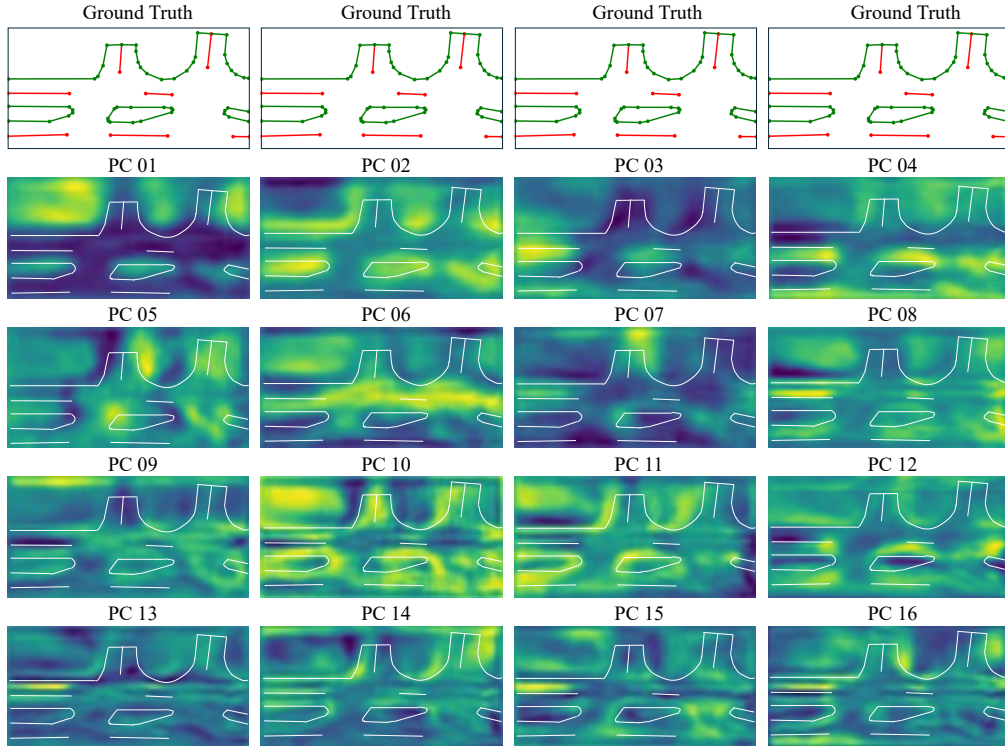


(b) AugMapNet

Figure 10. Example scene 1: Top 16 Principal Components of latent BEV grid of (a) StreamMapNet and (b) AugMapNet. Vector map ground truth is visualized at the top of each column as well as overlaid as white lines to ease the assessment of spatial accuracy. Notice that StreamMapNet tends to have radial artifacts.



(a) StreamMapNet



(b) AugMapNet

Figure 11. Example scene 2: Top 16 Principal Components of latent BEV grid of (a) StreamMapNet and (b) AugMapNet. Vector map ground truth is visualized at the top of each column as well as overlaid as white lines to ease the assessment of spatial accuracy. Notice that StreamMapNet tends to have radial artifacts.

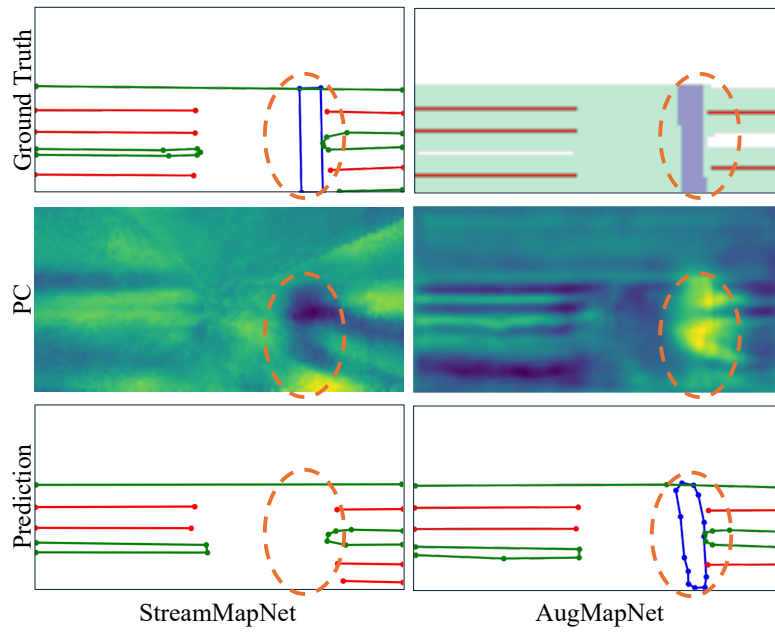


Figure 12. Extension of Fig. 4, visualizing example scene 1 where pedestrian crossing is missed by StreamMapNet but predicted by AugMapNet. PC is the Principal Component of the BEV latent grid that has the highest visual correspondence to the pedestrian crossing out of the top 16 Principal Components visualized in Fig. 10. It is PC 14 for StreamMapNet and PC 8 for AugMapNet, suggesting that this “crossing” PC is stronger in AugMapNet than StreamMapNet.